

# Energy and Latency of Beamforming Architectures for Initial Access in mmWave Wireless Networks

C. Nicolas Barati, Sourjya Dutta, Sundeep Rangan and Ashutosh Sabharwal

**Abstract**—Future millimeter-wave (mmWave) systems, 5G cellular or WiFi, must rely on highly directional links to overcome severe pathloss in these frequency bands. Establishing such links requires the mutual discovery of the transmitter and the receiver potentially leading to a large latency and high energy consumption. In this work, we show that both the discovery latency and energy consumption can be significantly reduced by using fully digital front-ends. In fact, we establish that by reducing the resolution of the fully-digital front-ends we can achieve lower energy consumption compared to both analog and high-resolution digital beamformers. Since beamforming through analog front-ends allows sampling in only one direction at a time, the mobile device is “on” for a longer time compared to a digital beamformer which can get spatial samples from all directions in one shot. We show that the energy consumed by the analog front-end can be four to six times more than that of the digital front-ends, depending on the size of the employed antenna arrays. We recognize, however, that using fully digital beamforming post beam discovery, i.e., for data transmission, is not viable from a power consumption standpoint. To address this issue, we propose the use of digital beamformers with low-resolution analog to digital converters (4 bits). This reduction in resolution brings the power consumption to the same level as analog beamforming for data transmissions while benefiting from the spatial multiplexing capabilities of fully digital beamforming, thus reducing initial discovery latency and improving energy efficiency.

**Index Terms**—Millimeter wave, Beamforming, Energy Consumption, Beam Discovery, Initial Access

## I. INTRODUCTION

Almost all of the current wireless communication takes place in a relatively small region of the electromagnetic spectrum below 6 GHz. This region has been allocated by government agencies around the world for commercial, civilian, military, public safety and experimental use. However, the proliferation of devices and services that use or depend on wireless technologies has caused an ever-increasing discrepancy between the demand and the available bandwidth, or degrees of freedom (DoF). This discrepancy termed *spectrum crunch*, if not addressed, will lead to lower data rates and reduced quality of service. Spectrum crunch will become even more acute when Internet of Things [39] and Device to Device communication traffic are added to the already overloaded networks.

Increasing the DoFs is the only option for the next generation (5G) wireless systems. The use of mmWave enables

an increase in DoFs by adding more bandwidth due to the availability of large (in the order of a few GHz) unlicensed spectrum between 30 and 300 GHz. However, as explained by Friis’ law [41], signals transmitted in mmWaves have high isotropic pathloss, i.e., they decay at a much higher rate with the traveled distance. This leads to a reduced communication range compared to sub-6 GHz systems. Furthermore, mmWaves exhibit characteristics resembling the visible light. For example, they have high penetration loss through most material and hence are easily blocked by the surrounding objects. MmWave systems can overcome these shortcomings by employing beamforming (BF). That is, to use arrays of multiple antenna elements to extend the communication range and avoid obstacles in the environment by directing the signal energy in an intended direction.

However, the reliance of mmWave communication on directional links through beamforming poses new challenges that do not exist in wireless systems over the microwave bands. The transmitter (Tx) and the receiver (Rx) must first discover each other directions before they can start the data communication. This process, known in cellular systems as *initial access*, is generally performed omni-directionally (or using very wide beams) in the sub-6 GHz bands. But, due to the high path loss, if mmWave systems were to follow the same paradigm, the range of mutual discovery would be much smaller than the range where directional high-rate communication would be possible. Therefore, mutual discovery must be performed in a directional manner.

The directional discovery phase can last for a long time when the base-station and the user employ arrays with many antenna elements forming narrow beams. While searching for the base-station, the battery-limited user is always “on” burning energy. We show here that this energy consumption can be reduced significantly by employing a low-resolution fully digital front-end on the user side. The reason is, beamforming through a digital front-end reduces the discovery latency (or delay) by an order of magnitude compared to an analog front-end. Hence, the user is “on” for a shorter span of time leading to considerable energy savings.

While the focus of this paper is directional discovery in initial access, directional discovery is expected to be triggered also in other phases of mmWave communication. For example, in recovery from link failures, which will be frequent due to the sensitivity of the mmWave links to obstacles and changes in the environment. Handovers to a new base-station will also be frequent since mmWave cells will be smaller in size compared to the current ones and a mobile user may go through more cells for the same distance traveled. More

---

C. Nicolas Barati (email: nicobarati@rice.edu) and Ashutosh Sabharwal (email: ashu@rice.edu) are with the Department of Electrical and Computer Engineering, Rice University, Houston, TX. Sourjya Dutta (email: sdutta@nyu.edu), Sundeep Rangan (email: srangan@nyu.edu), are with the NYU WIRELESS, Tandon School of Engineering, New York University, Brooklyn, NY.

importantly, since the battery-dependent devices operate at such high frequencies and bandwidth, more aggressive use of sleep/idle mode (discontinuous reception) will be critical from an energy consumption standpoint. For each of these operations, the user device must often (re-) discover the direction to the connected and neighboring base-station(s). Therefore, it is extremely crucial that directional discovery and beam alignment is fast and energy-efficient.

### A. Contributions

In this paper, we look into the problem of latency and energy consumption in directional discovery in mmWave systems during initial access. Our focus is on 5G cellular systems where the issue of communication range is more important and challenging than short-range mmWave communication, e.g., 802.11ad WiFi. There are two key take-away points in our work:

1. Digital beamforming results in both low latency and low energy consumption during initial discovery compared to analog beamforming.
2. Employing low resolution analog to digital converters (ADCs) in fully digital front-ends can achieve low latency and even lower power consumption for both control signalling and data transmissions.

Mutual directional discovery requires the transmitter and the receiver search in their surrounding angular space at a granularity inversely proportional to the size of their antenna arrays: larger antenna arrays result in narrower beams potentially leading to higher discovery delays. In a cellular environment, this latency will also affect user handovers between different base-stations, alternative link discovery in case of blockage and the “idle mode” to “on mode” circles.

We show that due to the large latency in directional discovery incurred by analog beamforming, its energy consumption is greater not only than low-resolution digital but also than high-resolution digital. This difference in energy consumption increases with the size of the antenna arrays. When a 4-by-4 antenna array is used, analog beamforming burns as much as six times more energy than digital. This is due to the fact that analog beamforming needs more time to sample an angular domain that increases in size with the number of antennas.

Leveraging our previous work [11], [12], we establish a relationship between the beamforming architecture, and the mutual discovery delay within the context of 3GPP initial access for mmWave networks [5]. Specifically, we show that between analog and digital beamforming, digital outperforms analog by a large margin – in the order of 300 to 900ms. Similar to [20] and [21], we detail and compare the power consumption of four beamforming architectures, namely, analog, digital, low-resolution digital and hybrid, by assessing the components and devices they are comprised of. It is known that by reducing the resolution of analog to digital converters (ADC) we can significantly reduce the power consumption of a fully digital beamforming circuit. However, we show that while this reduction comes at a penalty of less than 1 dB SNR in the low-SNR regime, the discovery delay is kept at the same low levels as digital beamforming with high resolution

– 20 to 80 ms. Thus, low resolution fully digital beamformers outperform analog as they can be power efficient during both data transmissions as well as signaling control messages.

Interestingly, in most studies related to mmWaves systems analog beamforming has been preferred over digital due to its low device power consumption. However, as we show, when discovery delay in initial access is taken into account, analog beamforming can burn multiple times more energy than any other alternative.

### B. Related Work

Due to the reliance on highly directional links at mmWave frequencies, efficient beam management is key to establishing and maintaining a reliable link. A critical component of beam management is the beam discovery procedure for initial access. Current technical literature assumes an analog or hybrid front-end which limits the number of usable spatial streams. For instance, [18], [37] present a heuristic method to design beam patterns for initial beam discovery for hybrid beamformers. Raghavan et al. in [40] proposes to vary the beam widths depending on the user link quality. They show that users with good link (high SNR) can be detected with wide beams leading to a decrease in detection delays. In another direction of research, [29], [31], [53] aim at designing optimal beam codebooks, i.e., sets of directions, for connection establishment. Another important area of research has been the use of *side information*, for instance location information, channel quality measurements at microwave bands, etc., has been studied in [6], [14], [15], [19], [23], [25], [34], [38], [51]. Moreover, the work in [44] propose the use of online machine learning algorithms for beam detection for vehicular communications at mmWave. The works in [33], [42], [54] use Game theoretic methods whereas in [27], [48] the authors use genetic algorithms for initial beam discovery.

In [9] the authors present a theoretical analysis of the trade-off between spending resources for accurate beam alignment on one hand and using them for actual data communication on the other. More interestingly, the analysis in [9] shows that with large coherence block lengths, exhaustive beam search outperforms hierarchical search. This understanding is reflected in the current 3GPP specifications [2]–[5] on initial access where initial beam discovery and alignment is achieved through exhaustive search. We will discuss the 3GPP New Radio beam search procedure briefly in Sec. II-B. A detailed overview of the beam management procedure for 5G systems can be found in [26].

Critical to beam discovery and beam alignment is the efficient signaling of pilot or synchronization signals and channel estimation. To this end, the work in [22], leverages the sparsity of the mmWave channel. The authors use a compressed sensing framework for estimating the number of measurements necessary for estimating the channel covariance matrix for beam/angle detection with high confidence. Similarly, in [47] compressed sensing is used for fast angle of arrival/departure and second-order channel statistics estimation. In [52] a compressed sensing-based algorithm robust to frequency offsets and phase noise is presented. The sparsity of the mmWave

channel is exploited in [13] where a novel algorithm based on multiple-armed bandit beam selection for both initial beam alignment and beam tracking is proposed. In [28], Hashemi *et. al.* exploit the channel correlation to reduce the searching space and subsequently the delay of beam discovery.

To better understand the interplay between the hardware (and power) constraints at mmWave and the beam discovery delay, in our previous work [11] [12], we presented a comparative analysis of analog and digital beamforming in terms of synchronization signal detectability and delay. We show that digital beamforming, even with low-resolution quantizers, performs dramatically better compared to analog or hybrid. Furthermore, our recent work, [20] and [21], presents a thorough study of various beamforming architectures at both the transmitter and the receiver sides. There, we show that employing losses in system rate under practical mmWave cellular assumptions. Based on this, we argue that as low-resolution fully digital front-ends can have *low control delays* while having the same power efficiency as analog and hybrid beamformers for the *data plane*. To the best of our knowledge, this is the first work where energy consumption during initial beam discovery has been studied. In this work, we show that a low resolution fully digital beamformer is energy efficient in both control plane in general, initial access in particular, and data plane.

The rest of the paper is organized as follows. In Sec. II we give an overview of the beam discovery problem and present the 3GPP New Radio (NR) discovery procedure. In Sec. III we present the system model. We derive a correlation-based detector for beam discovery, present four mmWave beamformers and comment on the power consumption of each one of them. In Sec. IV, we evaluate through simulations the performance of the analog and high/low-resolution beamformers in terms of discovery delay and energy consumption.

*a) Notation:* We use bold-face small letters ( $\mathbf{h}$ ) to denote vectors and bold-face capital letters ( $\mathbf{H}$ ) for matrices. Conjugate and conjugate transpose are denoted with  $\mathbf{h}^*$  and the  $\ell$ -2 norm with  $\|\mathbf{h}\|$  and  $\|\mathbf{H}\|$  for vectors and matrices, respectively.

## II. BEAM DISCOVERY THROUGH BEAMSWEEP

Consider a transmitter-receiver pair operating in mmWave bands. Since they communicate through directional links, they both must *discover* each other in the spatial domain before the data communication can begin. An intuitive approach to this problem is to divide the spatial domain around the transmitter (or receiver) into multiple non-overlapping sectors, as presented in Fig. 1a. Each of these sectors corresponds to a transmitter or receiver beam. All possible combinations of the pair of transmitter-receiver beams is termed as the *beamspace*. By increasing the number of antennas makes the beams narrower which increases the beamforming gain but also makes the size of the beamspace larger. This poses a fundamental problem for mmWave systems. On one hand, narrow beams are necessary for usable link budgets. On the other, beam discovery, i.e., finding the two matching beam pairs at the transmitter and the receiver, a difficult problem.

In this work, we assume a stand-alone communication model where the transmitter and the receiver are not assisted by out-of-band information regarding timing or position. The non-stand-alone model has been investigated in [6], [14], [15], [19], [23], [25], [34], [38], [51] and is not discussed in this work. There are two main approaches to beam discovery/selection under this assumption. One, called *beamsweep*, requires both the transmitter and the receiver to exhaustively search over the entire beamspace by measuring the received power for every possible transmitter-receiver beam pair. In another, the receiver side starts listening on the channel with the widest possible beam and step by step converges to the narrowest one. This is called hierarchical search, see Fig. 1b.

Both these techniques assume that a known signal called the *synchronization signal* in cellular, is transmitted periodically and the receiver will have to determine the direction in the beamspace where the incoming signal is stronger. While hierarchical search in principle is superior to beamsweep in terms of search delay [17], mmWave standards for both WiFi and cellular have adopted a beamsweep based procedure due to its simplicity [30] and [2]–[5]. In this work, we will also follow the beamsweep paradigm and our analysis and results are derived based on this assumption.

### A. Effect of beamforming on the beamspace

Under the beamsweep assumption, the effective size of the beamspace is a function of the beamforming scheme employed at the transmitter and the receiver. That is, the beamforming scheme dictates how many directions the receiver can inspect in a single observation. There are three beamforming schemes:

*Digital Beamforming:* In this architecture, each antenna element is connected to a radio frequency (RF) chain and a pair of data converters, analog to digital or digital to analog converters (ADC or DAC). The beamforming (or spatial filtering) is performed by the digital baseband processor. For wide-band systems with a large number of antennas, this architecture can have high power consumption when high precision DACs and ADCs are used. One way to use digital beamformers at mmWave is to use DACs and ADCs with few bits of quantizer resolution. This is attractive for beamformed systems as having digital samples from every antenna element allows the receiver to inspect theoretically infinite directions at the same time with full directional gain during only one observation of the channel. This reduction of the number of needed observations becomes significant as the beamspace grows and can potentially reduce the total power consumed during the search procedure.

*Analog Beamforming:* To avoid the use of a large number of DACs and ADCs, analog beamformers perform beamforming (or spatial filtering) on the analog (in RF or intermediate frequency) signal using RF phase shifters and power combiners (or splitters). The use of just a pair of ADCs considerably reduces the power consumed by these front-ends and hence, these are considered a prime candidate for initial mmWave based cellular devices. However, analog beamformers can point their beams only

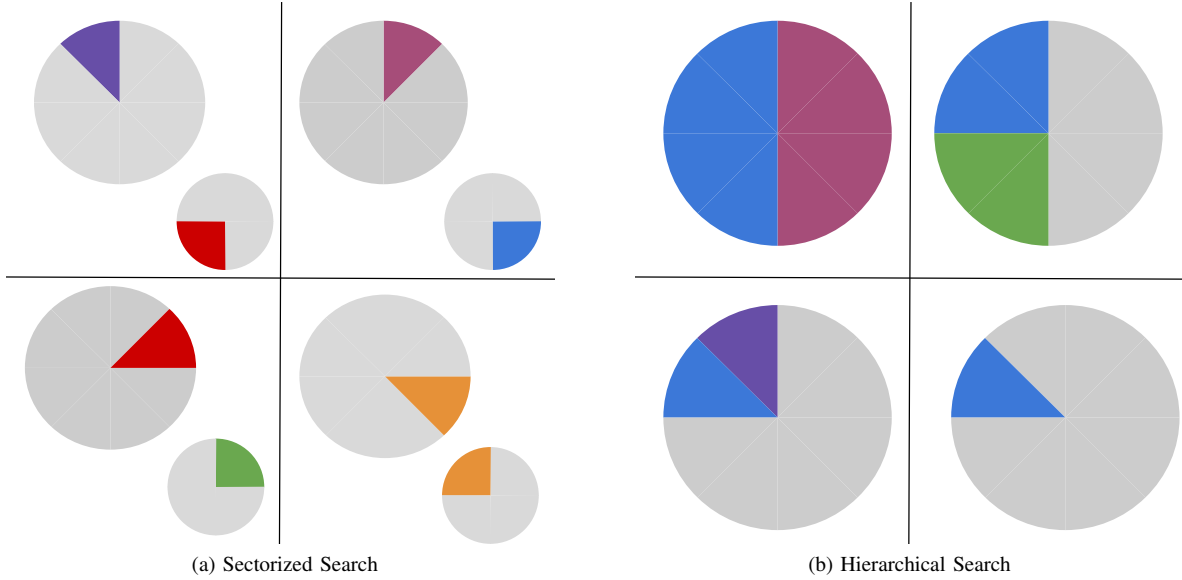


Fig. 1: Beam discovery in mmWave bands. Panels read from left to right and top to bottom. Fig. (1a) Search over narrow sectors. the receiver, larger shape, and the transmitter, smaller shape, sequentially visit each sector combination until mutual discovery. Fig. (1b) Hierarchical search. the receiver gradually narrows its beams in a series of steps.

in one direction at a given time. This leads to potentially high delays when the beamspace is large.

*Hybrid Beamforming:* This scheme is a combination of the digital and analog beamforming. A part of the beamforming is performed by  $M$  analog RF beamformers. These beamformed signals are digitized and combined (or precoded) by the digital baseband circuitry. This allows the receiver to inspect  $M$  directions at each time instance. Now, at an extreme  $M = 1$ , where we have analog beamforming. At the other,  $M$  equals the number of antenna elements, where the scheme is effectively digital beamforming. Choosing  $M$  trades off spatial multiplexing capabilities on the one hand, and energy consumption on the other.

Consider a transmitter equipped with an antenna array comprised of  $N_{Tx}$  antenna elements and a receiver equipped with  $N_{Rx}$  elements. This means that the size of the beamspace is equal to the product of  $N_{Tx}$  by  $N_{Rx}$ . If they both use analog beamforming, then, they must visit all these directions at  $N_{Tx} \times N_{Rx}$  separate channel inspections. Hence, the effective size of the beamspace is,

$$\text{analog: } L_{an} = N_{Tx} \times N_{Rx}. \quad (1)$$

Now, suppose that the transmitter still uses analog beamforming but the receiver uses digital. Then, the receiver can “listen on” all the  $N_{Tx}$  directions at once and hence in this effective case the size of the beamspace becomes

$$\text{digital: } L_{di} = N_{Tx}. \quad (2)$$

Applying the same logic, for hybrid beamforming, it is easy to see that the effective size of the beamspace is

$$\text{hybrid: } L_{hy} = \frac{N_{Tx} \times N_{Rx}}{M} \quad (3)$$

Other combinations of beamforming schemes on either the transmitter or the receiver yield an effective beamspace of various sizes. Adopting one beamforming scheme versus the other has a fundamental impact on the effective beamspace. This, in turn, affects the time needed for the receiver to determine the best direction of the incoming signal. Furthermore, during beamsweeping the receiver FE is *always on*. An FE architecture that can listen on one or a few directions at a time will hence need to be powered on for a longer period of time to measure all the possible beam pairs. This can mean a considerable increase in the effective power consumed by analog and hybrid beamformers. In the next sections we quantify the impact of the size of the beamspace and the choice of the beamformers on the energy consumed by beam discovery procedure.

### B. The 3GPP NR paradigm

As an illustrative example of a system using beamsweep, we will discuss the 3GPP NR physical layer standard for initial access (IA). Our analysis and results in the proceeding sections will all have an NR system as an underlying assumption. We chose NR for two reasons. One, it is the standard defined for 5G cellular systems so it is expected to be adopted by millions of devices in the coming years. Two, the NR standard offers a well-defined set of assumptions regarding the beam discovery process and time and frequency numerology. This allows us to evaluate the different beamforming schemes with respect to energy consumption within a widely accepted context.

We next present the beam discovery process which is one of the basic steps of NR *initial access*, i.e., the procedure of establishing a link-layer connection between a base-station, referred to as NR 5G nodeB (gNB) in the NR standard, and a mobile device or user equipment (UE).

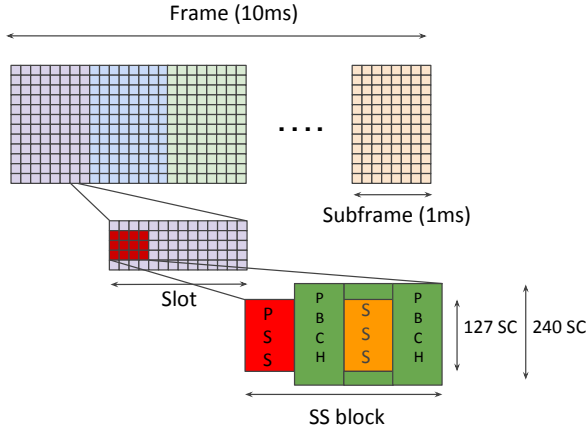


Fig. 2: Frame structure of 3GPP NR. A frame is divided into 10 subframes, a subframe into 8 slots and a slot into 14 OFDM symbols. A single SS block takes up 4 OFDM symbols.

1) *NR beam discovery*: Initial access involves a set of message exchanges between the gNB and the user equipment, whereby the user equipment identifies a serving gNB and synchronizes to it. The user equipment learns the physical cell identity of the gNB, sends back its own ID and finally attaches to the cell. In this work we will focus only on the first part of NR initial access: beam and cell discovery on the user equipment side, since this is the most critical in terms of detection delay and energy consumption.

On the gNB side, all the  $N_{TX}$  directions are swept with a periodicity of  $T = 20$  ms. More specifically, every  $T$  and for an interval of duration  $T_{ssb} = 5$  ms, the gNB transmits  $B$  blocks of four OFDM symbols in  $N_{TX}$  directions. These transmissions during  $T_{ssb}$  are called a synchronization signals (SS) burst and each block of the four OFDM symbols, an SS block. Each SS block is comprised of the primary synchronization signal (PSS), the secondary synchronization signal (SSS) and the physical broadcast channel (PBCH). The PSS and the SSS together make up the physical ID of the cell. The first one takes one of three possible values among  $\{0, 1, 2\}$  while the latter, one of  $\{0, 1, \dots, 335\}$ , resulting in a total of 1008 unique cell IDs. Each of these signals takes up 127 sub-carriers in frequency, while an entire SS block, including PBCH, 240 sub-carriers. In Fig. 2 we depict the time-frequency resources occupied by the SS block within an NR frame, subframe and slot.

Fig. 3 shows an example of several SS blocks within a single SS burst. For the mmWave bands, the NR standard provisions a total of  $B = 32$  SS blocks during each SS burst. It is assumed that each SS block is transmitted simultaneously in two directions using hybrid beamforming. Hence, a mmWave gNB can support up to 64 non-overlapping directions. As an example, in Fig. 4, we depict a scenario of a gNB beamsweeping  $N_{TX} = 8$  directions using  $B = 4$  SS blocks per SS bursts.

Now, the user equipment is also sweeping  $N_{RX}$  directions in searching for SS burst, see Fig. 4. These signals are known to the user equipment. It has to determine which one of the

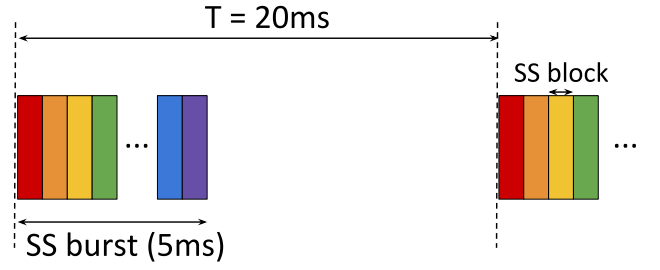


Fig. 3: SS burst. Each burst lasts for 5ms and is repeated every 20ms. Each SS block within an SS burst is shown in a different color.

possible three PSS sequences and 336 SSS sequences were sent. Since the structure of an SS block is also known, once the PSS is detected and the optimal direction is found, the user equipment will move on to detecting the SSS within the same SS block which is the next to the next OFDM symbol, as shown in Fig. 2. Thus, the most critical part of beamsweeping is the detection of the PSS which unlocks all the remaining steps of initial access.

The user equipment is assumed to use analog beamforming. Hence, unlike the gNB it can probe only one direction at a time. Since the gNB sends the SS blocks in two directions simultaneously, according to Sec. II-A the effective size of the beamspace around the gNB and the user equipment is  $L = (N_{TX} \times N_{RX}) / 2$ .

### III. SIGNAL AND SYSTEM MODEL

We will leverage the NR beam discovery process described earlier for our analysis and modeling, with a few simplifying assumptions. We consider a single cell of radius  $d_r$  with the gNB situated at the center transmitting the PSS signals periodically. The user equipment, through analog beamforming will sweep  $N_{RX}$  directions sequentially in search of the PSS signal.

Our first simplification is assuming analog beamforming at the gNB. Therefore, the user equipment and the gNB together will have to sample a beamspace of size  $L_{ang} = N_{tx} \times N_{rx}$ . Note that for user equipment at low SNR, i.e., those at the edge of the cell, it may be needed to cycle through the beamspace more than once. We will denote each cycle with  $k = 1, 2, \dots, K$ .

Our next assumption is that, similar to [12], the dominant path between the gNB and the user equipment is a line of sight (LOS) path aligned with exactly one of the transmitter-RX directions/sectors  $\ell^*$  in the beamspace. Although this assumption may seem unrealistic, since real channels are seldom comprised of a single path, it is only used to derive our detectors below. In our evaluation and simulations, we will test our detectors using a channel model derived from real measurements [8].

With these assumptions in mind, we model the received post-analog-BF received complex signal  $\mathbf{y}_{k\ell}$  at the user equip-

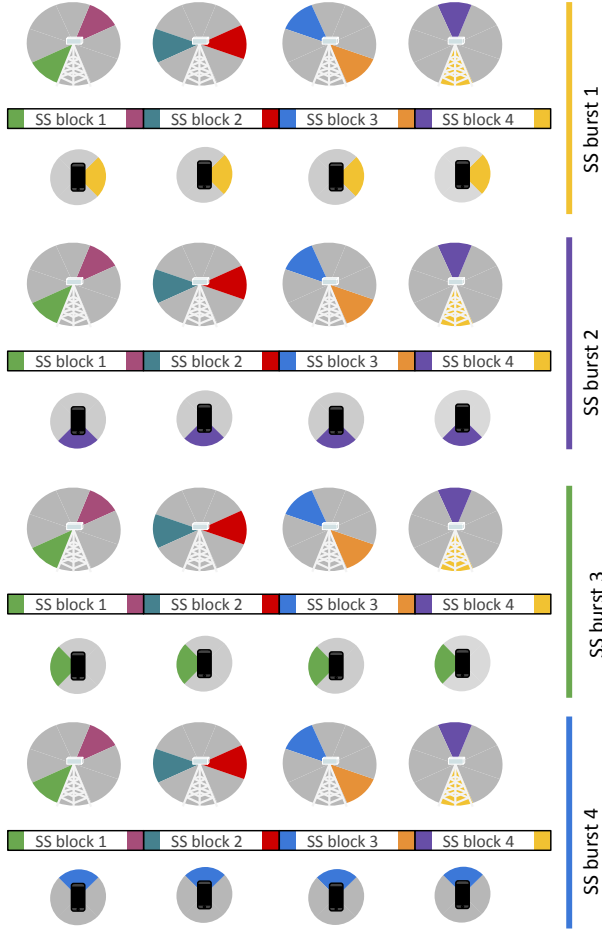


Fig. 4: Example of beam discovery within four SS bursts. During each SS burst, the gNB covers  $N_{\text{Tx}} = 8$  directions in 4 SS blocks. The user equipment on the other hand scans all the  $N_{\text{Rx}} = 4$  directions in four SS bursts. Thus, the user equipment and the gNB together need four SS bursts to cover the beamspace of size  $L = 16$ .

ment during the  $\ell$ -th sampling of the beamspace and  $k$ -th sweeping cycle as:

$$\mathbf{y}_{k\ell} = \mathbf{u}_{k\ell}^* \mathbf{H}_{k\ell} \mathbf{v}_{k\ell}^* \mathbf{x} + \mathbf{n}_{k\ell}, \quad \mathbf{n}_{k\ell} \sim \mathcal{CN}(0, \sigma_{k\ell}^2 \mathbf{I}_D). \quad (4)$$

The transmitted PSS signal  $\mathbf{x} \in \mathbb{C}^D$  is in a signal space with  $D \approx T_{\text{PSS}} \times W_{\text{PSS}}$  orthogonal degrees of freedom, where  $T_{\text{PSS}}$  and  $W_{\text{PSS}}$  are the PSS duration in time and bandwidth occupied by the PSS signal, respectively. We assume the PSS signal to be unit norm,  $\|\mathbf{x}\| = 1$ . The vectors  $\mathbf{u}_{k\ell} \in \mathbb{C}^{N_{\text{Rx}}}$  and  $\mathbf{v}_{k\ell} \in \mathbb{C}^{N_{\text{Tx}}}$  are, respectively, the user equipment and gNB side beamforming vectors along a transmitter-receiver direction  $\ell$  in the sectorized beamspace at the  $k$ -th sweep cycle. They are assumed to be of fixed-norm.

The MIMO channel  $\mathbf{H}$  is assumed to be flat-fading within the PSS bandwidth and constant over the PSS transmission time  $T_{\text{PSS}}$ . It is defined as

$$\mathbf{H} = h_{k\ell} \mathbf{u}_{\ell^*} \mathbf{v}_{\ell^*}^*, \quad (5)$$

where  $h_{k\ell}$  is a small-scale fading coefficient. The vectors  $\mathbf{u}_{\ell^*}$  and  $\mathbf{v}_{\ell^*}$  are the spatial signatures of the user equipment and

the gNB antenna arrays describing a single LOS path between them, aligned with only one of the transmitter-RX directions in the beamspace. They are given as

$$\begin{aligned} \mathbf{u}_{\ell^*} &= [1, e^{-j2\pi\Delta \cos(\phi_{\ell^*}^{\text{Rx}})}, \dots, e^{-j2\pi\Delta(N_{\text{Rx}}-1) \cos(\phi_{\ell^*}^{\text{Rx}})}]^T \\ \mathbf{v}_{\ell^*} &= [1, e^{-j2\pi\Delta \cos(\phi_{\ell^*}^{\text{Tx}})}, \dots, e^{-j2\pi\Delta(N_{\text{Tx}}-1) \cos(\phi_{\ell^*}^{\text{Tx}})}]^T, \end{aligned} \quad (6)$$

where  $\phi_{\ell^*}^{\text{Rx}}$  and  $\phi_{\ell^*}^{\text{Tx}}$  are the angles of arrival and departure in the directions of  $\ell^*$ , and  $\Delta$  is the distance between elements of the antenna arrays measured in wavelengths. Finally,  $\mathbf{n}$  in (4) is the i.i.d. complex additive white Gaussian noise vector with co-variance  $\sigma_{k\ell}^2 \mathbf{I}_D$ , and  $\mathbf{I}_D$  is the  $D \times D$  identity matrix.

The aim of the user equipment and the gNB is to mutually steer their beams along their spatial signatures defined in (6). That is, to apply beamforming vectors,  $\mathbf{u}_{\ell}$  and  $\mathbf{v}_{\ell}$ , as close to  $\mathbf{u}_{\ell^*}$  and  $\mathbf{v}_{\ell^*}$  as possible. This, based on our models in eq. (4) and eq. (5) and our fixed-norm assumption over the beamforming vectors, leads to the maximization of the energy of the received signal vector  $\mathbf{y}_{k\ell}$ .

#### A. Signal Detection

Given the signal and transmission model above we now derive the PSS detector through hypothesis testing. We will follow the same line of analysis given in [12]. Since we have assumed that the dominant path from the gNB to the user equipment is along a single transmitter-receiver beamspace direction  $\ell^*$  (here the asterisk denotes the true or best direction), for each probed direction in each sweeping cycle our null hypothesis,  $H_0$ , is that the signal is not present. Conversely, our alternative hypothesis,  $H_1$ , is that the signal is present, i.e., the user equipment is probing the direction in which the gNB is transmitting. Hence, eq. (4) under  $H_0$  (signal not present) and  $H_1$  (signal present at correct beamspace direction) becomes

$$\begin{aligned} H_0 : \mathbf{y}_{k\ell} &= \mathbf{n}_{k\ell} \\ H_1 : \mathbf{y}_{k\ell} &= \alpha_{k\ell^*} \mathbf{x} + \mathbf{n}_{k\ell^*}, \end{aligned} \quad (7)$$

where the scalar channel coefficient  $\alpha_{k\ell^*}$  is the result of applying the beamforming vectors along the spacial signatures of the user equipment and the gNB and is given by

$$\alpha_{k\ell^*} = \mathbf{u}_{\ell^*}^* \mathbf{H}_{k\ell^*} \mathbf{v}_{\ell^*} = h_{k\ell^*} \mathbf{u}_{\ell^*}^* \mathbf{u}_{\ell^*} \mathbf{v}_{\ell^*}^* \mathbf{v}_{\ell^*}. \quad (8)$$

We define the probability density of the received signal  $\mathbf{y}$  under the two hypotheses as  $p(\mathbf{y}|H_i, \alpha, \sigma^2, \ell^*)$  for  $i = \{0, 1\}$ , where the set  $\mathbf{y}$  contains all the observed signals  $\mathbf{y}_{k\ell}$  in  $K$  beam sweeps. The model contains several unknown parameters, namely,  $\alpha$  the set of all the channel coefficients  $\alpha_{k\ell^*}$ , and  $\sigma^2$  the set of all noise power levels.

Due to these unknown parameters, we will rely on the widely used generalized likelihood ratio test (GLRT) method [49]. The GLRT takes the likelihood distribution under each hypothesis maximized with respect to the unknown parameters and compares their ratio to a threshold. Alternatively, we can use the minimum log-likelihoods of the signal distribution under each hypothesis. These are given as

$$\Lambda_0 := \min_{\sigma^2} -\ln p(\mathbf{y}|H_0, \sigma^2) \quad (9a)$$

$$\Lambda_1 := \min_{\sigma^2, \alpha} -\ln p(\mathbf{y}|H_1, \sigma^2, \alpha). \quad (9b)$$

We then use the test

$$\Lambda := \Lambda_0 - \Lambda_1 \underset{H_0}{\overset{H_1}{\geq}} \theta \quad (10)$$

for a threshold  $\theta$ . We observe that under the assumption that the noise vectors are independent in different measurements,

$$\ln p(\mathbf{y}|H_0, \boldsymbol{\sigma}^2, \ell^*) = \sum_{k=1}^K \sum_{\ell=1}^L \ln p(\mathbf{y}_{k\ell} | \sigma_{k\ell}^2, \ell^*) \quad (11a)$$

$$\ln p(\mathbf{y}|H_1, \boldsymbol{\sigma}^2, \boldsymbol{\alpha}, \ell^*) = \sum_{k=1}^K \sum_{\ell=1}^L \ln p(\mathbf{y}_{k\ell} | \sigma_{k\ell}^2, \alpha_{k\ell^*}, \ell^*). \quad (11b)$$

Therefore, the negative log-likelihoods in eq.(9) can be rewritten as

$$\Lambda_0 = \sum_{k=1}^K \sum_{\ell=1}^L \Lambda_0^{k\ell}(\ell^*). \quad (12a)$$

$$\Lambda_1 = \sum_{k=1}^K \sum_{\ell=1}^L \Lambda_1^{k\ell}(\ell^*), \quad (12b)$$

where  $\Lambda_0^{k\ell}(\ell^*)$  and  $\Lambda_1^{k\ell}(\ell^*)$  are the minimum negative log-likelihoods in each measurement and given as:

$$\Lambda_0^{k\ell}(\ell^*) = \min_{\sigma^2} -\ln p(\mathbf{y}_{k\ell} | \sigma_{k\ell}^2, \ell^*). \quad (13a)$$

$$\Lambda_1^{k\ell}(\ell^*) = \min_{\sigma^2, \alpha_{k\ell}} -\ln p(\mathbf{y}_{k\ell} | \sigma_{k\ell}^2, \alpha_{k\ell}, \ell^*). \quad (13b)$$

Since the received signal in our model, given by eq. (7), is Gaussian conditional on the parameters, hence

$$-\ln p(\mathbf{y}_{k\ell} | \sigma_{k\ell}^2, \ell^*) = \frac{1}{\sigma_{k\ell}^2} \|\mathbf{y}_{k\ell}\|^2 + D \ln(\pi \sigma_{k\ell}^2) \quad (14)$$

under the  $H_0$  hypothesis, and

$$-\ln p(\mathbf{y}_{k\ell} | \sigma_{k\ell}^2, \alpha_{k\ell^*}, \ell^*) = \frac{1}{\sigma_{k\ell}^2} \|\mathbf{y}_{k\ell} - \alpha_{k\ell^*} \mathbf{x}\|^2 + D \ln(\pi \sigma_{k\ell}^2) \quad (15)$$

under the  $H_1$  hypothesis. Now, we use the above eqns. (14) and (15), to obtain estimates of the unknown variables which are their minimizers.

We first take  $\Lambda_1^{k\ell}(\ell^*)$ . The channel coefficient  $\alpha_{k\ell^*}$  that minimizes the log negative likelihood when the signal is present is given as

$$\hat{\alpha}_{k\ell^*} = \frac{\mathbf{x}^* \mathbf{y}_{k\ell}}{\|\mathbf{x}\|^2}. \quad (16)$$

Next we move on to minimize over the variance  $\sigma^2$ , which occurs at

$$\hat{\sigma}_{k\ell}^2 = \frac{1}{D} \left( \|\mathbf{y}_{k\ell}\|^2 - \frac{|\mathbf{x}^* \mathbf{y}_{k\ell}|^2}{\|\mathbf{x}\|^2} \right). \quad (17)$$

When the signal is not present, i.e.,  $\ell \neq \ell^*$ , we minimize  $\Lambda_0^{k\ell}(\ell^*)$  over the variance  $\sigma^2$ . The minimum is obtained at

$$\hat{\sigma}_{k\ell}^2 = \frac{\|\mathbf{y}_{k\ell}\|^2}{D}. \quad (18)$$

Substituting eq.(16), eq.(17) and eq. (18), in eq. (13) we obtain

$$\Lambda_0^{k\ell}(\ell^*) = D \ln \left( \frac{\pi e}{D} \|\mathbf{y}_{k\ell}\|^2 \right), \quad (19a)$$

$$\Lambda_1^{k\ell}(\ell^*) = D \ln \left( \frac{\pi e}{D} \left( \|\mathbf{y}_{k\ell}\|^2 - \frac{|\mathbf{x}^* \mathbf{y}_{k\ell}|^2}{\|\mathbf{x}\|^2} \right) \right) \quad (19b)$$

Combining (19) and from the test (10), and eq. (12) we have the following log-likelihood difference

$$\Lambda = \sum_k \sum_{\ell} -D \ln(1 - \rho_{k\ell}), \quad (20)$$

where the  $\rho_{k\ell}$  is the normalized energy of the correlation of the known signal with the received signal, obtained as

$$\rho_{k\ell} = \frac{|\mathbf{x}^* \mathbf{y}_{k\ell}|^2}{\|\mathbf{x}\|^2 \|\mathbf{y}_{k\ell}\|^2}.$$

This, not surprisingly, means that while the user equipment probes each direction in  $K$  beamsweeps, it should correlate the incoming signal with the local replica of the known signal. Then, since eq. (20) is an increasing function of  $\rho_{k\ell}$ , and due to our assumption that the signal is present only in one direction within the beamspace, the best direction  $\hat{\ell}^*$  is the one in which the correlation was the highest, that is,

$$\hat{\ell}^* = \arg \min_{\ell=1, \dots, L} \sum_k \sum_{\ell} \ln(1 - \rho_{k\ell}). \quad (21)$$

While the above detector was derived for analog beamforming under favorable beamspace assumptions, it can also be used for both hybrid and digital beamforming. The difference is that with these beamforming architectures, the receiver has access to  $N_{RF} > 1$  RF chains and can essentially operate as  $N_{RF}$  parallel analog systems. In the digital beamforming case  $N_{RF}$  is equal to  $N_{RX}$ . Note that with a fully digital detector the receiver can test all the angles, including those not perfectly aligned in the beamspace. However, for the sake of simplicity and better comparison with analog beamforming, we will not consider a more powerful detector but assume that in digital beamforming too the arrival angles are aligned with the beamspace directions.

## B. RF Architectures and power consumption

While standards documents on the implementation of mmWave cellular systems assume user equipments with analog beamforming and only a single RF chain, we believe that there is much value in using fully digital beamforming. To make our case more concrete in terms of energy consumption we give here an overview of the receiver's mmWave front-end. We model the power consumption of analog, hybrid and fully digital and fully digital with low-resolution quantization front ends.

### 1) mmWave front-ends :

a) *Analog front-end*:: Consider the mmWave receiver's analog front-end shown in Fig. 5. It is comprised of  $N_{RX}$  low noise amplifiers (LNA)s,  $N_{RX}$  phase shifter (PS), a mixer, a combiner and a pair of analog to digital converter (ADC). The D.C. power consumption of each LNA,  $P_{DC}^{LNA}$  is a function of

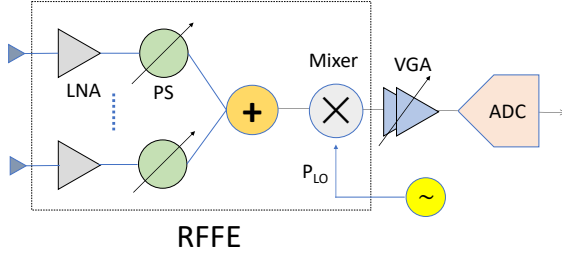


Fig. 5: Analog beamforming receiver architecture.

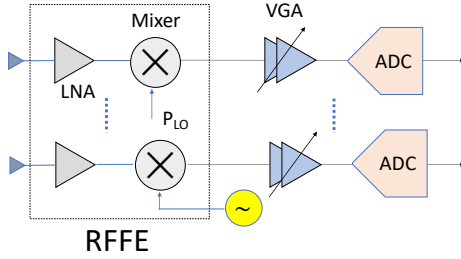


Fig. 6: Digital beamforming receiver architecture.

its gain  $G_{LNA}^{PS}$ , the noise figure  $N_{LNA}$  and the figure of merit (FoM) and is given as [7], [21], [46]

$$P_{LNA}^{DC} = \frac{G_{LNA}^{PS}}{\text{FoM}(N_{LNA} - 1)}, \quad (22)$$

in linear scale.

The PS and mixer are considered to be passive elements. While they do not burn any power, they do however introduce insertion losses (IL), which need to be compensated for. For example, the LNA gain above needs to be high enough to offset the loss introduced by the phase shifter  $IL_{PS}$ . That is, if an LNA in a circuit without any PS had a gain  $G_{LNA}$ , then  $G_{LNA}^{PS} = G_{LNA} + IL_{PS}$ .

For the ADCs, the power consumption is a function of the sampling frequency  $F_s$ , ADC's figure of merit and the resolution in bits:

$$P_{ADC} = \text{FoM} \times F_s \times 2^q, \quad (23)$$

where  $q$  is the number of resolution bits. To keep the variable incoming signal within the ADCs dynamic range while keeping a constant baseband power  $P_{BB}^{out}$  it is necessary to apply gain control to the input of the ADC. This is performed by the variable gain amplifier (VGA) with a gain range between 0 and  $G_{VGA}^{max}$ . For the analog beamforming case this maximum gain is calculated as:

$$G_{VGA}^{max} = \frac{P_{BB}^{out} - 10 \log(N_{RX}) + IL_{mix}}{-(G_{LNA}^{PS} - IL_{PS}) - P_{RX}(d = d_{max})}, \quad (24)$$

where  $IL_{mix}$  is the insertion loss introduced by the mixer and  $P_{RX}(d = d_{max})$  is the maximum distance between the transmitter and the receive, i.e., the cell edge.

Given the above gain, the D.C. power draw of the VGA is given as

$$P_{VGA}^{DC} = \frac{G_{VGA}^{max} F_s}{\text{FoM} A_{chip}}, \quad (25)$$

Where FoM is the FoM of the VGA,  $F_s$  the sampling bandwidth in GHz and  $A_{chip}$  is the active area in  $\text{mm}^2$ .

Based on the above, the total power consumption of an analog mmWave front-end can be calculated as

$$P_{an} = N_{RX} P_{LNA}^{DC} + P_{LO} + P_{ADC} + P_{VGA}^{DC}, \quad (26)$$

where  $P_{LO}$  is the power draw of the local oscillator.

b) *Digital front-end*:: Consider the digital front-end in Fig. 6. Since we have introduced most of the components in the analog front-end case, computing the power for the digital case much easier. Notice in the figure, that since beamforming is done in baseband there is no need for phase shifters. Neither do the LNA gains need to compensate for their insertion losses. Therefore, we will use  $G_{LNA}$  instead of  $G_{LNA}^{PS}$ . However, the number of the ADCs is increased to  $N_{RX}$ , so is the number of VGAs, mixers and local oscillators. Thus, the DC power draw by the LNA and VGA are given as

$$P_{LNA}^{DC} = \frac{G_{LNA}}{\text{FoM}(N_{LNA} - 1)}, \quad (27)$$

and

$$G_{VGA_{dig}}^{max} = \frac{P_{BB}^{out} - 10 \log(N_{RX}) + IL_{mix}}{-(G_{LNA}) - P_{RX}(d = d_{max})}. \quad (28)$$

With these, the total power consumed by a fully digital mmWave front-end is

$$P_{dig} = N_{RX}(P_{LNA}^{DC} + P_{LO} + P_{ADC} + P_{VGA_{dig}}^{DC}). \quad (29)$$

c) *Digital front-end with low quantization ADCs*:: The front-end here remains the same as in Fig. 6. The only thing that changes is the resolution  $q$  of the ADCs. Notice in eq. (23), that the power consumption is exponential in  $q$ . Since the power consumption of a fully digital mmWave front-end grows linearly in the number of antenna elements  $N_{RX}$  as given in eq. (29), reducing the resolution is the only meaningful way of bringing the power draw of a fully digital front-end. In our calculations below and in Section IV we will show how reducing the quantization resolution affects both the power draw of the front-end and the energy consumption during the beam discovery process.

d) *Hybrid front-end*:: For the sake of completeness, we also present the mmWave hybrid front-end in Fig.7. There are a few options in designing a hybrid front-end. Here, we show the "industry-standard" sub-array architecture where the antenna array is divided by the number of supported digital streams. The depicted front-end can support  $M = 2$  digital streams each connected to sub-arrays of size  $N_{rm,RX}/2$ . Notice that this circuit has elements from both the fully digital and analog front-ends:  $N_{RX}$  phase shifters and  $M = 2$  pairs of ADCs. Thus, the total power consumption of the hybrid front-end is



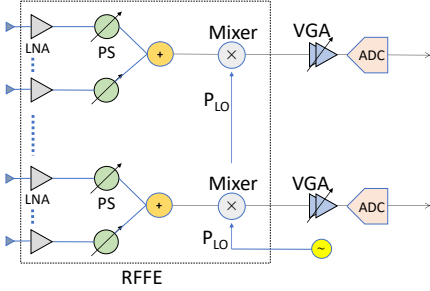


Fig. 7: Sub-array hybrid beamforming receiver architecture.

$$P_{hy} = N_{RX} P_{LNA}^{DC} + M(P_{LO} + P_{ADC} + P_{VGA}^{DC}). \quad (30)$$

2) *front-end power consumption*: To give a better picture of each front-end's power consumption, we will now give numerical examples. We will use power draws and losses of individual components as reported in studies in the literature and give a total number for each front-end when put together.

For an LNA with gain  $G_{LNA} = 10$  dB with a noise figure of  $N_{LNA} = 3$  dB and  $FoM = 6.5mW^{-1}$  we have used the 90 nm CMOS LNA reported in [7], [21], [46]. We have assumed a PS insertion loss  $IL_{PS} = 10$  dB which the analog front-end LNA gain  $G_{LNA}^{PS}$  needs to compensate for.

For the ADC, we have used a 4-bit Flash-based ADC reported in [36] with an  $FoM$  of 67.6fJ/conversion step. While the 4-bit ADC falls into the category of a low-resolution ADC, we use the same architecture and  $FoM$  for higher a quantization of  $q = 10$  bits for better comparison.

For the VGA, we consider the 90nm CMOS reported in [50]. The VGA's  $FoM$  is 5280 for an active area of  $0.01mm^2$ . Last, we have assumed an oscillator power draw of 10 dBm, a mixer insertion loss of  $IL_{mix}$  of 6 dBm and baseband power  $P_{BB}^{out}$  of 10 dBm.

Using the above device properties, we, furthermore, consider an operating bandwidth ( $BW$ ) of 400 MHz, the maximum provisioned bandwidth by 3GPP NR and a maximum distance  $d_{max}$  of 100 meters. We then use the channel model [8] to calculate the pathloss needed for computing the received power  $P_{RX}$  in eq. (24) and (28). Specifically, for an EIRP Tx power of 43 dBm the received power is  $-87$  dBm at  $d_{max}$  where the channel is expected to be non-line-of-sight (NLOS). Finally, we assume a sampling rate,  $F_s = 1$  GHz and a receiver array size of  $N_{RX} = 16$ . While we assume a system bandwidth of 400 MHz, however, according to the NR specifications OFDM sampling rate is set at 491 MHz. Furthermore, we consider an oversampling rate at  $2\times$  the system bandwidth to avoid aliasing. Hence, the 1 GHz sampling rate assumption.

By plugging the above numbers into (22) – (30), we obtain the front-end power consumption presented in Table I. With the term RFFE we denote the Radio Frequency front-end which is the pre-VGA part of the mmWave front-end, i.e., the LNAs and the LO. We observe a couple of points:

- The power consumption of a high-resolution digital front-end is almost six times the consumption of the analog

front-end. However, it is below a factor of  $N_{RX}$ . This is because while there are  $N_{RX}$  ADCs in a digital front-end, there are also  $N_{RX}$  phase shifters in an analog one, the insertion loss of which must be compensated by the LNAs. We will see in the next section how the gap between analog and digital closes when we take into account the beam discovery delay.

- Reducing the ADC resolution from  $q = 10$  to  $q = 4$  bits has a dramatic effect on the power consumption. It is in fact even below that of the analog front-end. However, this reduction in resolution adds a distortion to the signal which will reduce the effective SNR. This reduction has a small effect in the low to median SNR regimes. [20], [21].

#### IV. EVALUATION AND SIMULATION

We now evaluate the performance of our correlation-based detector for receivers performing analog, fully digital and low-resolution fully digital beamforming. In a series of steps, we first define the simulation setup and parameters, assess the effect of lowering the quantization resolution in fully digital front-ends, and finally illustrate the interplay between the beamspace and the energy consumption of each the front-end architectures presented in Section III.

##### A. Channel model and user SNR distribution

We consider a single cell of radius  $d_r = 100$  m, with the mmWave base-station, or gNB, situated at the center. We then randomly drop user equipments in this cell and compute their pathloss to the gNB according to the widely used model in [8]. This urban multipath model is based on real measurements in 28 GHz bands performed in New York City [10], [32], [43], [55]. While our detector was derived for a single-path LOS channel perfectly aligned with one of the beamspace directions, we will use this multipath channel in our evaluation and simulations. According to this model, links between the user equipment and the gNB are in LOS or NLOS based on an exponential probability distribution parametrized by the distance separating the two,  $d$ . Close user equipments have a high probability of being in LOS while as the distance grows the probability of being in NLOS increases. The resulting omni-directional pathloss, i.e., before applying beamforming, in dB is computed as

$$P_L = \mu + 10\nu \log_{10}(d) + \zeta [\text{dB}], \quad \zeta \sim \mathcal{N}(0, \xi^2), \quad (31)$$

where  $\mu$ ,  $\nu$  and  $\xi^2$  are parameters defined by whether the link is LOS or NLOS.

We then use this pathloss to derive the user equipment omni-directional SNR,  $SNR_{omni}$  as

$$SNR_{omni} = \frac{P_{RX}}{N_0 W_{sys}}, \quad (32)$$

where  $P_{RX}$  is the received omni directional power resulted from subtracting the pathloss in (31) from the transmitted power  $P_{TX}$ . The remaining parameters above are the noise

TABLE I: mmWave Receiver's Power Consumption (mW). A receiver array size of 16 antennas and a sampling rate of 1GHz are assumed.

front-end Architecture	RFFE	VGA	ADC ( $q = 10$ )	ADC ( $q = 4$ )	Total
Analog	257.3	1.55	133.12	–	391.97
Hybrid ( $M = 2$ )	267.3	3.1	266.24	–	536.64
Digital (High res.)	184.7	24.8	2129.9	–	2339.4
Digital (Low res.)	184.7	24.8	–	33.28	242.78

TABLE II: SNR distribution parameters.

Parameter	Value	Description
$d_r$	100 m	Cell radius
$P_{TX}$	30 dBm	gNB TX power
$NF_{UE}$	7 dB	user equipment noise figure
$kT$	-174 dBm/Hz	Thermal noise power density
$F_c$	28 GHz	Carrier Frequency
$W_{sys}$	400 MHz	System bandwidth
$P_{LOS}(d)$	$\exp(-a_{los}d)$ , $a_{los} = 67.1$ m	Probability of LOS vs. NLOS
$P_{NLOS}(d)$	$1 - P_{LOS}(d)$	Probability of NLOS
$PL(d)$	$\mu + 10\nu \log_{10}(d) + \zeta$ , $\zeta \sim \mathcal{N}(0, \xi^2)$	Path loss model dB, $d$ in meters
$\mu_{LOS}, \nu_{LOS}, \xi_{LOS}$	$\mu = 61.4, \nu = 2.0, \xi^2 = 5.8$ dB	LOS parameters
$\mu_{NLOS}, \nu_{NLOS}, \xi_{NLOS}$	$\mu = 72.0, \nu = 2.92, \xi^2 = 8.7$ dB	NLOS parameters

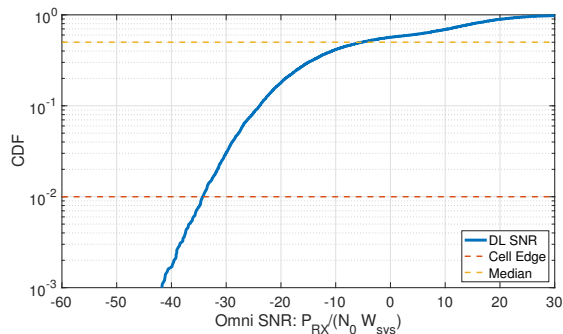


Fig. 8: SNR distribution of 10,000 user equipment drops

power density plus noise figure,  $N_0$ , and the system bandwidth  $W_{sys}$ .

Next, we derive the user equipments SNR distribution through 10,000 random drops in our cell and divide them into three regimes: cell edge user equipments, i.e., the first percentile of the CDF, median users and above, and those in between these regimes. However, in the sequel, we characterize the energy consumed by the analog and digital beamformers during beam discovery for the cell edge and the median users. Fig. 8 shows the CDF of the SNR distribution. A summary of the parameters and their values used to derive this distribution is presented in Table II.

### B. Low-resolution fully digital beamforming

In section III-B, we presented the power consumption of four mmWave front-ends implementing analog, hybrid and fully digital beamforming. We also showed that the power consumption of the fully digital front-end can be dramatically reduced by employing low-resolution ADCs.

However, reducing the resolution will degrade the quality of the received signal. We quantify this degradation by using the method presented in [11], [16], [24]. According to [24], the effect of low-resolution quantization, i.e., analog to digital

conversion, is modeled as a reverse gain  $(1 - \gamma)$  multiplied with the received sample if it had gone through an infinite-resolution quantizer and an additive Gaussian noise term. That is if the high quantization sample is given as

$$y[n] = x[n] + w[n],$$

where  $x[n]$  are the transmitted signal sample and  $w[n]$  AWG noise with some variance  $\mathbb{E}|w[n]|^2 = \sigma_n^2$ , then the imperfectly quantized received sample is given as

$$y_q[n] = (1 - \gamma)x[n] + (1 - \gamma)w[n] + v[n]. \quad (33)$$

The last term  $v[n]$  is a zero-mean Gaussian random variable with the following variance [11], [24]

$$\sigma_q^2 = \mathbb{E}|v[n]|^2 = \gamma(1 - \gamma)(\mathbb{E}|x[n]|^2 + \sigma_n^2). \quad (34)$$

Now, using eq. (33) the effective SNR  $\text{SNR}_{\text{eff}}$  after quantization is obtained as

$$\text{SNR}_{\text{eff}} = \frac{(1 - \gamma)\text{SNR}_{\infty}}{1 + \gamma\text{SNR}_{\infty}},$$

where  $\text{SNR}_{\infty}$  is the SNR value of an infinite-resolution quantizer. The value of  $\gamma$  depends on the quantizer's design, the input distribution and the quantization resolution bits  $q$ . As an example, for a Gaussian input the value of  $\gamma$  is only 0.01.

Thus, we see that low-quantization fully digital beamforming comes with a penalty in the SNR, an observation corroborated by the theoretic work in [35] and [45]. However, this penalty can be negligible depending on the quantization bits  $q$ , and the SNR regime, as shown in [20] and [21], where the same model was used for OFDM inputs. The effective SNR can be much lower, though, for very high values of  $\text{SNR}_{\infty}$  at very low quantization bits, say one or two. However, in cellular systems, the overwhelming majority of user equipments are at low to medium SNR regimes where the distance between the effective SNR and  $\text{SNR}_{\infty}$  is below 3 dB. Furthermore,

at a quantization of  $q = 4$  bits as we consider for our low-resolution fully digital front-end, even at  $\text{SNR}_\infty$  as high as 20 dB the effective SNR is still below 3 dB [20], [21].

### C. System parameters

We will compare the mmWave front-ends presented in Section III, within the context of 3GPP NR's PSS discovery. We assume a PSS signal that is confined within one OFDM symbol and 127 sub-carriers. For a sub-carrier spacing of  $\Delta_f = 120\text{kHz}$ , they are  $8.91\mu\text{s}$  and  $15.24\text{ MHz}$ , respectively. We will assume that the channel is almost flat within the duration and bandwidth of the signal.

Both the user equipment and the gNB are equipped with uniform planar arrays that allow them to beamsteer in both azimuth (az) and elevation (el). Note that from now on we note the available directions at the gNB and user equipment with  $N_D^{\text{Tx}}$  and  $N_D^{\text{Rx}}$ , respectively. These are the products of  $N_D^{\text{Tx}}$  and  $N_D^{\text{Rx}}$  in each dimension of the 2D arrays. Hence, the beamspace size  $L$  is equal to  $N_D^{\text{Tx}} \times N_D^{\text{Rx}}$ . The gNB is assumed to perform only hybrid beamforming with  $M = 2$  directions at a time, while the user equipment may employ one of analog, fully digital and low-resolution fully digital beamforming. Note that we keep the transmission power of the gNB fixed at 30 dBm (Table II). Therefore, transmitting the PSS in  $M = 2$  directions implies that the sum of the power transmitted in each direction must be 30 dBm. We will assume equal power transmission. Thus, the signal in each direction will carry half of the total 30 dBm power. The resulting beamforming gains will be applied to the user equipments' omni-directional SNR given by eq. (32) and the effective SNR in case of the low-resolution digital front-end.

Also, we assume a beamspace discovery process as described in Section II-B1, where the gNB transmits the PSS directionally in its  $N_D^{\text{Tx}}$  direction within an SS burst of duration 5ms every  $T = 20$  ms. The user equipment also sweeps its  $N_D^{\text{Rx}}$  directions in search of one of the  $N_{\text{PSS}} = 3$  PSS sequences. Finally we compute the threshold  $\theta$  in test (10). We will do so through the false alarm probability  $P_{\text{FA}}$ . Suppose we would like to maintain a constant target false alarm rate of  $R_{\text{FA}}$  during each searching period. Then, the false alarm probability and the false alarm rate are connected through

$$P_{\text{FA}} = \frac{R_{\text{FA}}}{N_{\text{PSS}} N_{\text{dly}} N_{\text{FO}}}. \quad (35)$$

Now,  $N_{\text{dly}}$  is the number of delay hypotheses. That is at which delay  $\tau$  the signal was present. Since the PSS transmission is periodic, the number of the delays hypotheses is bounded and it is the number of the samples within each SS burst period. If the signal was present at a delay  $\tau_1$ , then it is also present at delay  $T + \tau_1$ , where  $T$  is the SS burst period.

To compensate for two other sources of uncertainty, we incorporate them into the  $P_{\text{FA}}$  calculation. These are the number of possible PSS sequences  $N_{\text{PSS}}$  and the number of frequency offsets hypotheses  $N_{\text{FO}}$ . There are  $N_{\text{PSS}}$  sequences that the user equipment may mistake one with the other two and are factored in the false alarm calculation. Next, we approximate

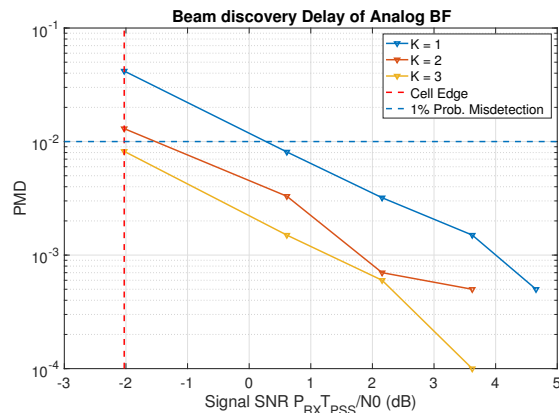


Fig. 9: Analog Receiver: Mis-detection vs Signal SNR.  $K = 1, 2, 3$  and  $P_{\text{MD}}^{\text{tgt}} = 1\%$ .

$N_{\text{FO}}$  as follows. First, we assume a local oscillator error of  $\pm 10$  parts per million (ppm) and a Doppler shift for a velocity up to 30 km/h at  $F_c = 28\text{ GHz}$ . The LO error and the Doppler shift will define a range  $\pm \Delta f_{\text{max}}$ . We then discretize this range so that in each interval the channel does not rotate more than  $\pi/4$  within the duration of one OFDM symbol. The number of frequency offset hypotheses is then the number of obtained intervals.

The threshold  $\theta$  therefore is the value of the normalized correlation  $\rho_{k\ell}$  which corresponds to the target  $P_{\text{FA}}$ . The detector will consider everything above this threshold as received signal and anything below as noise.

All the parameters described above are tabulated in Table III.

### D. Comparison of different beamforming architectures

Now that we have defined the channel model, system and signal parameters, and described the beamspace and beam discovery procedure, we can start the comparison between the mmWave front-ends presented in Section III-B. We first look into the beam discovery delays with beamsweeping for the beamformers and then tie these delays to the power consumptions reported in Section III-B2.

1) *Beamsweeping delay*: We estimate the initial discovery delay as the time needed to go through all the beams in the beamspace times the total number beamsweeps  $K$  necessary to determine the best direction for a target mis-detection probability  $P_{\text{MD}}^{\text{tgt}}$ . Hence,  $K$  is a function of  $P_{\text{MD}}^{\text{tgt}}$ . Since our detector is essentially an energy detector, maximizing energy of the incoming signal from the correct direction, depending on the SNR regime the user equipment may need to perform multiple sweeps. In Fig. 9 we show the number of beamsweeps necessary to discover the correct path to the gNB for a  $P_{\text{MD}}^{\text{tgt}} = 1\%$ . A mobile user at the cell edge needs  $K = 3$  beamsweeps to get the direction right, while the rest of the users can detect the signal in one beamsweep.

Take as an example the case of the analog receiver with  $N_D^{\text{Rx}} = 16$  directions. The size  $L$  of the beamspace is then  $16 \times 64 = 1024$ . Then, the initial discovery delay  $T_{\text{delay}}(P_{\text{MD}}^{\text{tgt}})$ ,

TABLE III: System parameters.

Parameter	Value
Total system bandwidth, $W_{sys}$	400 MHz
Signal Duration, $T_{PSS}$	8.91 $\mu$ s (1 OFDM symbol)
Sub-carrier spacing, $\Delta_f$	120kHz
PSS Bandwidth, $W_{PSS}$	15.24MHz (127 sub-carriers)
SS burst period, $T$	20ms
SS burst duration, $T_{ssb}$	5ms
Total false alarm rate per scan cycle, $R_{FA}$	0.01
Number of PSS waveform hypotheses $N_{PSS}$	3
Number of frequency offset hypotheses, $N_{FO}$	3
gNB antenna	$N_{TX} \times N_{TX}$ uniform planar array
UE antenna	$N_{RX} \times N_{RX}$ uniform planar array
gNB antenna elements in each dimension	$N_{rmTX} = 8$
UE antenna elements in the azimuth dimension	varies: $N_{RX}^{az} = 2, 4$
UE antenna elements in the elevation dimension	varies: $N_{RX}^{el} = 2, 4$
gNB directions	$N_D^{TX} = N_{TX} \times N_{TX} = 8 \times 8 = 64$
UE directions	varies $N_D^{RX} = N_{RX}^{az} \times N_{RX}^{el} = 4, 8, 16$
gNB beamforming	Hybrid $M = 2$
UE beamforming	Varied: Analog, Digital, low-res. Digital

TABLE IV: Upper bounds of initial discovery delays for different mmWave front-ends.  $P_{MD}^{tgt}$  is set to 1%.

front-end Arch.	Cell Edge Disc. Delay	Median User Disc. Delay
Analog	960 ms	320 ms
Digital (High res.)	60 ms	20 ms
Digital (Low res.)	80 ms	20 ms

for such a user equipment to successfully discover the true direction is

$$\begin{aligned}
\frac{(K(P_{MD}^{tgt}) - 1) \times L \times T}{N_D^{Tx}} + T_{ssb} &\leq T_{delay}(P_{MD}^{tgt}) \leq \\
&\leq \frac{K(P_{MD}^{tgt}) \times L \times T}{N_D^{Tx}} \\
&= \frac{20480K(P_{MD}^{tgt})}{64} \text{ms}, \quad (36)
\end{aligned}$$

where  $T = 20$  ms is the SS burst period and  $T_{ssb} = 5$  ms the duration of an SS burst. The reason we divided the quantity above with  $N_D^{Tx}$  is that within each SS burst period  $T$ , the gNB sweeps all its directions in one SS burst. Also, notice that we did not divide  $L$  by the number of the RF chains  $M = 2$  at the transmitter. Since the NR procedure defines a maximum of  $B = 32$  SS blocks within one SS burst and the number of directions the gNB scans is  $N_D^{Tx} = 64$ , the reduction in the effective beamspace due to hybrid beamforming is accounted for. Otherwise, dividing eq. (36) by  $M$  would imply that the user equipment probes  $M = 2$  directions directions each time, which is not correct since it employs an analog beamformer.

From eq. (36), we can see that even for a user that is not at the cell edge, i.e.,  $K(P_{MD}^{tgt}) = 1$ , the initial discovery delay can go as high as 320ms, when the entire control-plane delay of 4G LTE must be below 50ms [1]. For the cell edge user on the other hand, this delay is between 640 ms and almost a second. This highlights the large impact of the beamspace size on the initial discovery delay. Now, during initial discovery the user equipment must be constantly “on” searching for the correct beamspace. This amount of delay as we will show next

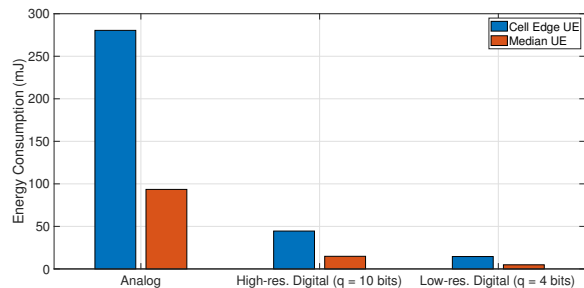


Fig. 10: Energy consumption of the mmWave front-ends: Analog, High-resolution Digital and Low-resolution Digital. Number of antenna elements at the user equipment  $N_{RX} = 16$ . Cell Edge user equipment in blue, Median user equipment in red.

has a large impact on the power consumption of the analog beamformer.

In Table IV following the same process and using eq. (36), we give the upper bounds of the initial discovery delay for the other two kinds of front-ends, fully digital and low resolution fully digital. All the numbers are for a user equipment array size of 16 elements. Notice that the SNR penalty due to low quantization is negligible in both the cell edge and the rest of the area. The large gain compared to analog was the result of shrinking the beamspace size  $L$  to only  $N_D^{Tx}$  which is all covered in one SS burst.

2) *Beamsweeping Energy consumption:* We have so far characterized the beam discovery delay of the analog, the high-resolution digital and the low-resolution digital beamformers. The energy consumption of a front-end is tightly connected to the amount of time it needs to operate. Since the user equipment is assumed to be always “on” trying to attach to a gNB, it is necessary to go beyond the device power consumption and look at energy consumption during the time needed to establish a directional link between the user equipment and the gNB. In Fig. 10 we show the energy consumption of the three front-ends, where the user equipment array size is  $N_{RX} = 16$ . The difference between analog and the two versions of digital is astonishing. The energy

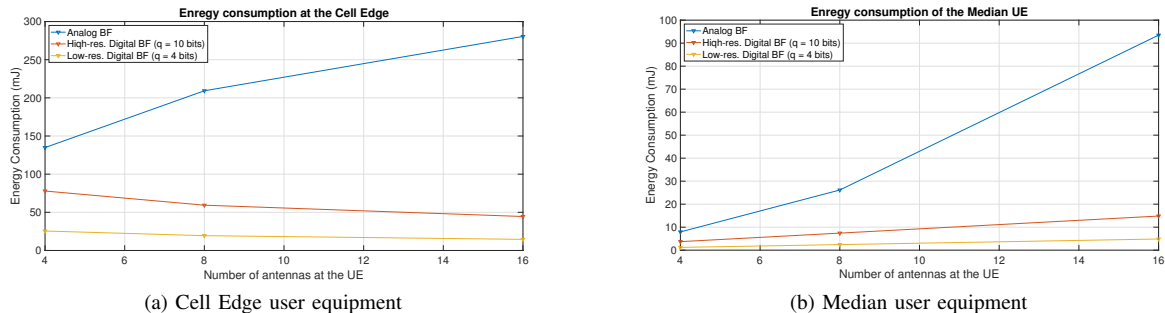


Fig. 11: Energy consumption as a function of the user equipment array size. Fig. (11a) Energy consumption at the cell edge. Fig. (11b) energy consumption of the median user equipment.

consumption of analog towers even that of high-resolution digital. Remember, when we looked at the front-ends' power consumption (Joules/s) in Section III-B2 digital beamforming's consumption was six times that of analog beamforming. What Fig. 10 shows though, is the analog beamforming front-end burning almost four times more energy than the high-resolution digital front end during beamsweeping.

However, since after establishing the directional link, in the data communication phase, analog is expected to burn less power than fully digital, we believe that mmWave systems will need to use a low-resolution fully digital front-end. Despite the fact that the difference in energy consumption between high and low-resolution digital front-ends is quite small during beam discovery.

Next, we turn our attention to the number of antenna elements at the receiver. We would like to know how the energy consumption scales with the size of the antenna array in the initial beamsweeping phase. In other words, what is the impact of various beamspace sizes on the energy consumption? Fig. 11 answers this question. We try three different configurations at the user equipment: a 2D array of size 4, a 2D array of size 8, and a 2D array of size 16. There are a few interesting points these two figures raise:

- o First, while fewer antennas do bring the energy consumption of the user equipment down, analog beamforming still burns considerably more energy than both the digital front-ends.
- o Second, the gap between analog and digital beamforming widens as more antennas are employed at the user equipment. The reason is the following: when the number of antennas is small, and the post-BF SNR is low, analog beamforming looks into a fewer directions at each period. This means that the most crucial factor in the front-ends' energy consumption is the size of the beamspace. This leads to higher beam discovery delays resulting in longer "on" time for the user equipment. This is more evident in Fig. 11b where all front-ends need no more than  $K = 1$  beamsweep to detect the true path to the gNB.
- o Related to the previous point, the value of digital beamforming is evident in every antenna configuration. The reduction in the size of the effective beamspace is the fundamental and necessary aspect of expediting beam discovery and subsequently, lowering energy consumption.

Beyond initial link establishment, digital beamforming will reduce the complexities involved in handovers and avoiding blockage in connected mode.

## V. CONCLUSION AND FUTURE DIRECTIONS

The realization of mmWave communication systems requires addressing two crucial challenges, namely beam discovery delay and energy consumption. In this work, we have revealed how closely these two are tied together. Specifically, we showed that employing analog beamforming can significantly increase both the discovery delay and, subsequently, energy consumption. Hence, analog beamforming does not buy us lower energy consumption.

Digital beamforming, on the other hand, achieves lower delays and lower energy consumption during beam discovery. In addition, depending on operating SNR, using digital beamforming can allow the use of multi-stream communication and allow joint flexible scheduling of frequency resources and directional beams. This may be extremely useful in the case of small data packets. By expediting beam discovery, fully digital may enable more aggressive use of sleep mode since beam tracking and paging can be less frequent. In fact, studying the effect of beamforming architectures on higher layers, i.e., MAC and TCP/IP, in a multi-cell setup is an interesting direction for future research.

It is true that when the directional data link is established, analog burns less energy compared to fully digital. Reducing the quantization resolution of the ADC pairs, however, can bring the energy requirements in data communication at the level of analog beamforming at a penalty negligible in most SNR regimes. Thus, low-resolution digital beamforming enables the realization of mmWave cellular systems with low discovery delays while allowing more flexible scheduling.

## REFERENCES

- [1] 3GPP: Requirements for Further Advancements for E-UTRA (LTE-Advanced). TR 36.913 (release 9) (2010)
- [2] 3GPP: NR – Physical Channels and Modulation. TS 38.211 (release 15) (2018)
- [3] 3GPP: NR–Physical Layer Measurements. TS 38.215 (release 15) (2018)
- [4] 3GPP: NR–Physical Layer Procedures for Control. TS 38.213 (release 15) (2018)
- [5] 3GPP: NR–Radio Resource Control (RRC) Protocol Specification. TS 38.331 (release 15) (2018)

- [6] Abbas, W.B., Zorzi, M.: Context information based initial cell search for millimeter wave 5g cellular networks. In: 2016 European Conference on Networks and Communications (EuCNC), pp. 111–116 (2016)
- [7] Adabi, E., Heydari, B., Bohsali, M., Niknejad, A.M.: 30 GHz CMOS low noise amplifier. In: Proc. IEEE RFIC Symp., pp. 625–628 (2007)
- [8] Akdeniz, M., Liu, Y., Samimi, M., Sun, S., Rangan, S., Rappaport, T., Erkip, E.: Millimeter wave channel modeling and cellular capacity evaluation. *IEEE J. Sel. Areas Commun.* **32**(6), 1164–1179 (2014)
- [9] Alkhateeb, A., Nam, Y., Rahman, M.S., Zhang, J., Heath, R.W.: Initial beam association in millimeter wave cellular systems: Analysis and design insights. *IEEE Trans. on Wireless Commun.* **16**(5), 2807–2821 (2017)
- [10] Azar, Y., Wong, G.N., Wang, K., Mayzus, R., Schulz, J.K., Zhao, H., Gutierrez, F., Hwang, D., Rappaport, T.S.: 28 GHz propagation measurements for outdoor cellular communications using steerable beam antennas in New York City. In: Proc. IEEE ICC (2013)
- [11] Barati, C.N., Hosseini, S., Rangan, S., Liu, P., Korakis, T., Panwar, S., Rappaport, T.S.: Directional cell discovery in millimeter wave cellular networks. *IEEE Trans. Wireless Commun.* **14**(12), 6664 – 6678 (2015)
- [12] Barati, C.N., Hosseini, S.A., Mezzavilla, M., Korakis, T., Panwar, S.S., Rangan, S., Zorzi, M.: Initial access in millimeter wave cellular systems. *IEEE Trans. Wireless Commun.* **15**(12), 7926–7940 (2016)
- [13] Booth, M.B., Suresh, V., Michelusi, N., Love, D.J.: Multi-armed bandit beam alignment and tracking for mobile millimeter wave communications. *IEEE Communications Letters* **23**(7), 1244–1248 (2019)
- [14] Capone, A., Filippini, I., Sciancalepore, V.: Context information for fast cell discovery in mm-wave 5g networks. In: Proceedings of European Wireless 2015; 21th European Wireless Conference (2015)
- [15] Capone, A., Filippini, I., Sciancalepore, V., Tremolada, D.: Obstacle avoidance cell discovery using mm-waves directive antennas in 5g networks. In: 2015 IEEE 26th Annual International Symposium on Personal, Indoor, and Mobile Radio Communications (PIMRC), pp. 2349–2353 (2015)
- [16] Chen, J.H., Gersho, A.: Gain-adaptive vector quantization with application to speech coding. *IEEE Trans. Commun.* **COM-35**(9), 918–930 (1987)
- [17] Chiu, S., Ronquillo, N., Javidi, T.: Active learning and csi acquisition for mmwave initial alignment. *IEEE J. Sel. Areas Commun.* **37**(11), 2474–2489 (2019)
- [18] De Donno, D., Palacios, J., Widmer, J.: Millimeter-wave beam training acceleration through low-complexity hybrid transceivers. *IEEE Transactions on Wireless Communications* **16**(6), 3646–3660 (2017)
- [19] Devoti, F., Filippini, I., Capone, A.: Mm-wave initial access: A context information overview. In: 2018 IEEE 19th International Symposium on "A World of Wireless, Mobile and Multimedia Networks" (WoWMoM), pp. 1–9 (2018)
- [20] Dutta, S., Barati, C.N., Dhananjay, A., Rangan, S.: 5G millimeter wave cellular system capacity with fully digital beamforming. In: Proc. Asilomar Conf. on S, S & C, pp. 1224–1228 (2017)
- [21] Dutta, S., Barati, C.N., Ramirez, D., Dhananjay, A., Buckwalter, J.F., Rangan, S.: A case for digital beamforming at mmwave. *IEEE Trans. Wireless Commun.* pp. 1–1 (2019)
- [22] Eliasi, P.A., Rangan, S., Rappaport, T.S.: Low-rank spatial channel estimation for millimeter wave cellular systems. *IEEE Trans. Wireless Commun.* **16**(5), 2748–2759 (2017)
- [23] Filippini, I., Sciancalepore, V., Devoti, F., Capone, A.: Fast cell discovery in mm-wave 5g networks with context information. *IEEE Transactions on Mobile Computing* **17**(7), 1538–1552 (2018)
- [24] Fletcher, A.K., Rangan, S., Goyal, V.K., Ramchandran, K.: Robust predictive quantization: Analysis and design via convex optimization. *IEEE J. Sel. Topics Signal Process.* **1**(4), 618–632 (2007)
- [25] Garcia, G.E., Seco-Granados, G., Karipidis, E., Wymeersch, H.: Transmitter beam selection in millimeter-wave mimo with in-band position-aiding. *IEEE Transactions on Wireless Communications* **17**(9), 6082–6092 (2018)
- [26] Giordani, M., Polese, M., Roy, A., Castor, D., Zorzi, M.: A tutorial on beam management for 3gpp nr at mmwave frequencies. *IEEE Communications Surveys Tutorials* **21**(1), 173–196 (2019)
- [27] Guo, H., Makki, B., Svensson, T.: A genetic algorithm-based beamforming approach for delay-constrained networks. In: 2017 15th International Symposium on Modeling and Optimization in Mobile, Ad Hoc, and Wireless Networks (WiOpt), pp. 1–7 (2017)
- [28] Hashemi, M., Sabharwal, A., Koksai, C., Shroff, N.: Efficient beam alignment in millimeter wave systems using contextual bandits. In: Proc. IEEE INFOCOM, pp. 2393–2401 (2018)
- [29] Hussain, M., Love, D.J., Michelusi, N.: Neyman-pearson codebook design for beam alignment in millimeter-wave networks. In: Proceedings of the 1st ACM Workshop on Millimeter-Wave Networks and Sensing Systems 2017, mmNets '17, pp. 17–22. ACM (2017)
- [30] IEEE: IEEE standard for information technology?telecommunications and information exchange between systems local and metropolitan area networks?specific requirements - part 11: Wireless lan medium access control (mac) and physical layer (phy) specifications. *IEEE Std 802.11-2016* (Revision of IEEE Std 802.11-2012) pp. 1–3534 (2016)
- [31] Jaesim, A., Siasi, N., Aldalbahi, A., Ghani, N.: Beam-bundle codebook for highly directional access in mmwave cellular networks. *IEEE Communications Letters* **23**(11), 2104–2108 (2019)
- [32] MacCartney, G.R., Samimi, M.K., Rappaport, T.S.: Exploiting directionality for millimeter-wave system improvement. In: International Conference on Communications (ICC), 2015 IEEE (2015)
- [33] Marandi, M.K., Rave, W., Fettweis, G.: Beam selection based on sequential competition. *IEEE Signal Processing Letters* **26**(3), 455–459 (2019)
- [34] Marciano, A.S., Christiansen, H.L.: Macro cell assisted cell discovery method for 5g mobile networks. In: 2016 IEEE 83rd Vehicular Technology Conference (VTC Spring), pp. 1–5 (2016)
- [35] Mo, J., Heath, R.W.: Capacity analysis of one-bit quantized MIMO systems with transmitter channel state information. *IEEE Trans. Signal Process.* **63**(20), 5498–5512 (2015)
- [36] Nasri, B., Sebastian, S.P., You, K.D., RanjithKumar, R., Shahrjerdi, D.: A 700 uW 1GS/s 4-bit folding-flash ADC in 65nm CMOS for wideband wireless communications. In: Proc. ISCAS, pp. 1–4 (2017)
- [37] Palacios, J., De Donno, D., Giustiniano, D., Widmer, J.: Speeding up mmwave beam training through low-complexity hybrid transceivers. In: 2016 IEEE 27th Annual International Symposium on Personal, Indoor, and Mobile Radio Communications (PIMRC), pp. 1–7 (2016)
- [38] Park, E., Choi, Y., Han, Y.: Location-based initial access and beam adaptation for millimeter wave systems. In: 2017 IEEE Wireless Communications and Networking Conference (WCNC), pp. 1–6 (2017)
- [39] Qualcomm Inc.: How will 5g transform industrial iot. Whitepaper available at <https://www.qualcomm.com/media/documents/files/how-5g-will-transform-industrial-iot.pdf>
- [40] Raghavan, V., Cezanne, J., Subramanian, S., Sampath, A., Koymen, O.: Beamforming tradeoffs for initial ue discovery in millimeter-wave mimo systems. *IEEE J. Sel. Topics Signal Process.* **10**(3), 543–559 (2016)
- [41] Rappaport, T.S.: *Wireless Communications: Principles and Practice*, second edn. Prentice Hall, Upper Saddle River, NJ (2002)
- [42] Rave, W., Khalili-Marandi, M.: The elimination game or: Beam selection based on m-ary sequential competition elimination. In: WSA 2019; 23rd International ITG Workshop on Smart Antennas (2019)
- [43] Samimi, M., Wang, K., Azar, Y., Wong, G.N., Mayzus, R., Zhao, H., Schulz, J.K., Sun, S., Gutierrez, F., Rappaport, T.S.: 28 GHz angle of arrival and angle of departure analysis for outdoor cellular communications using steerable beam antennas in New York City. In: Proc. IEEE VTC (2013)
- [44] Sim, G.H., Klos, S., Asadi, A., Klein, A., Hollick, M.: An online context-aware machine learning algorithm for 5g mmwave vehicular communications. *IEEE/ACM Transactions on Networking* **26**(6), 2487–2500 (2018)
- [45] Singh, J., Dabeer, O., Madhow, U.: On the limits of communication with low-precision analog-to-digital conversion at the receiver. *IEEE Trans. Commun.* **57**(12), 3629–3639 (2009)
- [46] Song, I., Jeon, J., Jhon, H., Kim, J., Park, B., Lee, J.D., Shin, H.: A simple figure of merit of RF MOSFET for low-noise amplifier design. *IEEE Electron Device Lett.* **29**(12), 1380–1382 (2008)
- [47] Song, X., Haghghatshoar, S., Caire, G.: A scalable and statistically robust beam alignment technique for millimeter-wave systems. *IEEE Trans. Wireless Commun.* **17**(7), 4792–4805 (2018)
- [48] Souto, V.D.P., Souza, R.D., Uchoa-Filho, B.F., Li, Y.: A novel efficient initial access method for 5g millimeter wave communications using genetic algorithm. *IEEE Transactions on Vehicular Technology* **68**(10), 9908–9919 (2019)
- [49] Van Trees, H.L.: *Detection, Estimation and Modulation Theory, Part I*. Wiley, New York, NY (2001)
- [50] Wang, Y., Afshar, B., Ye, L., Gaudet, V.C., Niknejad, A.M.: Design of a low power, inductorless wideband variable-gain amplifier for high-speed receiver systems. *IEEE Trans. Circuits and Syst. I: Reg Papers* **59**(4), 696–707 (2012)
- [51] Xiu, Y., Wu, J., Xiu, C., Zhang, Z.: Millimeter wave cell discovery based on out-of-band information and design of beamforming. *IEEE Access* **7**, 23076–23088 (2019)

- [52] Yan, H., Cabria, D.: Compressive sensing based initial beamforming training for massive mimo millimeter-wave systems. In: 2016 IEEE Global Conference on Signal and Information Processing (GlobalSIP), pp. 620–624 (2016)
- [53] Zhang, J., Huang, Y., Shi, Q., Wang, J., Yang, L.: Codebook design for beam alignment in millimeter wave communication systems. IEEE Transactions on Communications **65**(11), 4980–4995 (2017)
- [54] Zhang, Q., Saad, W., Bennis, M., Debbah, M.: Quantum game theory for beam alignment in millimeter wave device-to-device communications. In: 2016 IEEE Global Communications Conference (GLOBECOM), pp. 1–6 (2016)
- [55] Zhao, H., Mayzus, R., Sun, S., Samimi, M., Schulz, J.K., Azar, Y., Wang, K., Wong, G.N., Gutierrez, F., Rappaport, T.S.: 28 GHz millimeter wave cellular communication measurements for reflection and penetration loss in and around buildings in New York City. In: Proc. IEEE ICC (2013)